



Stress Redistribution of Headed Stud Connectors Subjected to Constant Shear Force

Rong Liu¹ · Zhiqiang Feng¹ · Hengda Ye¹ · Yuqing Liu²

Received: 11 January 2019 / Accepted: 1 November 2019 / Published online: 6 November 2019
© Korean Society of Steel Construction 2019

Abstract

In order to evaluate the stress concentration of stud shear connectors considering creep effect of concrete, finite element analysis of the push-out specimen is carried out. The rate of creep method is used in the solid model to reflect the creep property of concrete. Local bearing stress and splitting stress of concrete are analyzed. The stress concentration of steel beam and stud near the weld toe are obtained. Results show that owing to the creep effect of concrete, the local stresses of the stud are redistributed, even under constant shear force. The stress concentration factor (SCF) of concrete bearing stress in front of the weld collar decreases by about 52%, while the bending deformation of the stud increases due to the stress redistribution given 10 years of creep time. SCF at the weld toe of steel beam increases about 1.5 times of short-term, and SCF of stud shank increases about 3 times. The stress concentration at the root of studs become more obvious under constant shear force due to concrete creep, which is adverse for the long-term behavior of studs in the normal service stage.

Keywords Headed stud connectors · Creep · The rate of creep method · Stress concentration · Finite element analysis

1 Introduction

Steel–concrete composite structures aim to utilize steel members with high strength and light self-weight to resist tensile stress, and concrete blocks with high compressive strength and low material cost to resist compressive stress. It is able to reach a balance between extraordinary mechanical behavior and engineering cost. As a result, composite structures have been widely used in buildings and bridges (Ranzi et al. 2013).

The compatible coupling action between steel and concrete elements mainly depends on the connectors installed at the steel–concrete interface, such as rebars, angle channels, headed studs and perforated steel ribs. The stud is one of the most widely used shear connectors owing to its higher capacity, obvious ductility and orientation-independent in plane shear property. In short and moderate span composite girders bridges, studs are dominantly used to connect

concrete slabs and steel girders. In long-span cable-stayed bridges, studs are frequently used to connect the main girder of the steel mid-span and the pre-stressed concrete side-span (Liu and Liu 2015). Among the world's top 10 cabled-stayed bridges according to the span rank, eight bridges use studs in steel–concrete hybrid girders (Xu et al. 2013). Figure 1 shows the applications of studs in bridges. Studs are also used in the anchorage zone to connect steel anchorage box of stayed-cable and the concrete pylon in cable-stayed bridges (Liu et al. 2015). Studs are welded on the steel component and embedded into the concrete element to resist the potential steel–concrete slip and spalling in contemporary bridge structures. Generally, studs are crucial to the safety and durability of composite structures. Although studs in composite beams have achieved profound progress in several decades, especially when the special joints are considered, the behavior of studs is of vast interests in current research and practical application.

Several numerical and experimental studies are conducted previously to study the structural behavior of headed studs embedded in composite structural component with transverse sheeting. A variety of methods for modeling concrete and steel interaction using shear connectors were presented by Rahnavard et al. (2016, 2017, 2018, 2019). In their research, the B31 element type was used for shear

✉ Rong Liu
Liurong1983@hhu.edu.cn

¹ College of Civil and Transportation Engineering, Hohai University, Nanjing 210098, China

² Department of Bridge Engineering, Tongji University, Shanghai 200092, China

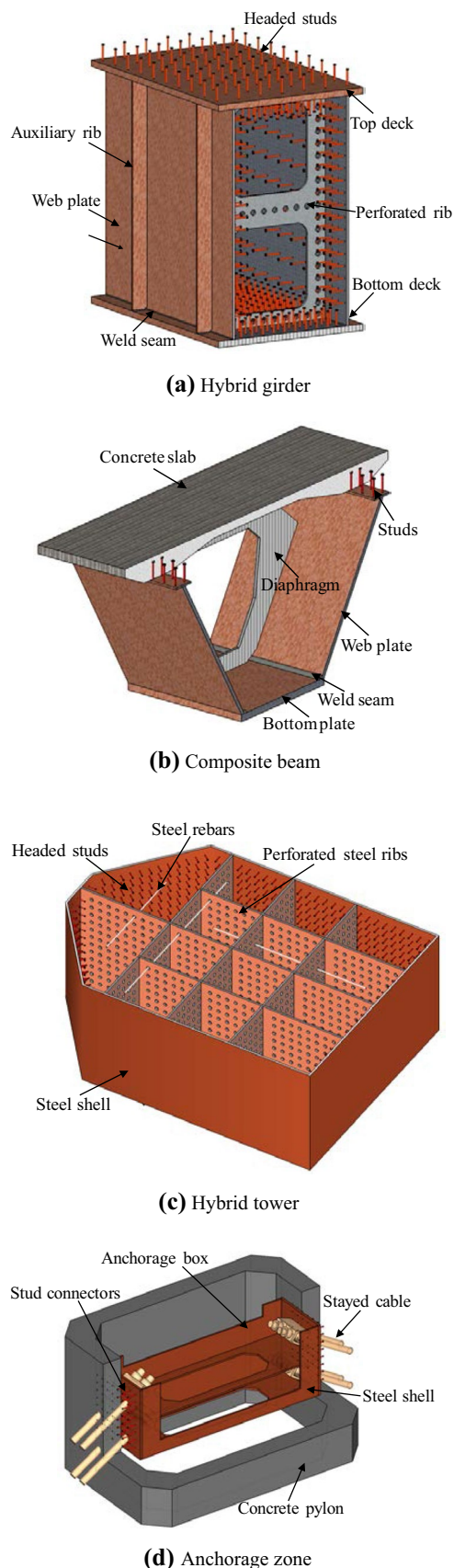


Fig. 1 Applications of studs in bridge engineering

connector modeling in composite shear walls (Rahnavard et al. 2016), composite connections (Rahnavard et al. 2019), buckling restrained braces (Naghavi et al. 2019; Rahnavard et al. 2018) and composite steel–concrete beam (Rahnavard et al. 2017). Moreover, numerical modeling of interaction between steel headed stud connectors and concrete using normal and tangential contact properties was presented by Shin et al. (2013, 2014).

Given long-term load cases are concerned, the stress redistribution between steel and concrete, owing to the creep property of concrete, may decrease the safety margin of composite structures. At serviceability limit state, concrete creep also significantly increases the deflection of composite bridges. In long-span bridges, the permanent load is up to 80% of the total. Thus, concrete creep effect mainly included by permanent loads should not be ignored in the design of composite members. Since the early applications of studs in bridges, numerous studies on studs have been carried out. Push-out tests, beam tests, theoretical analysis and finite element modeling of composite beams have been carried out to evaluate the long-term performance of composite beams (Al-deen et al. 2011; Ban et al. 2015; Huang et al. 2019; Mirza and Uy 2010). Previous researches provide a fundamental understanding of the long-term behavior of composite beams, and greatly improve the design and engineering applications of composite beams.

Even though the stud connector is the only reliable element to transmit forces between steel and concrete, limited studies concerning the long-term behavior of studs have been carried out. In most bridge design recommendations (MOHURD 2013; JRA 2002), the secondary shear force increment included by concrete creep is superimposed to other effects, and the load carrying capacity is only based on short-term test results. These design methods disagree with some long-term test results, that is, the load carrying capacity of stud decreases with the increased loading time. The long-term constant loaded studs subject to plastic failure near the weld collar, which implies that concrete creep decreases the ultimate shear capacity of those studs (Mirza and Uy 2010). Further study should be conducted to demonstrate the concrete creep effects on the long-term behavior of studs and its time-varying shear mechanism.

Spring models have been used to simulate studs under short-term loads and long-term loads in FEA studies of push-out tests and composite beams (Al-deen et al. 2011; Qi et al. 2017; Rahnavard et al. 2018). The overall behavior of composite members may be reflected using spring models, nevertheless, it is unable to reflect the local behavior of studs. Besides, the stiffness of spring elements needs to be determined first. Solid models are used to predict load carrying capacity of studs, and FEA results show good agreement with the test results (Bonilla et al. 2019; Guezouli et al. 2013; Han et al. 2017). Compared with spring models, solid

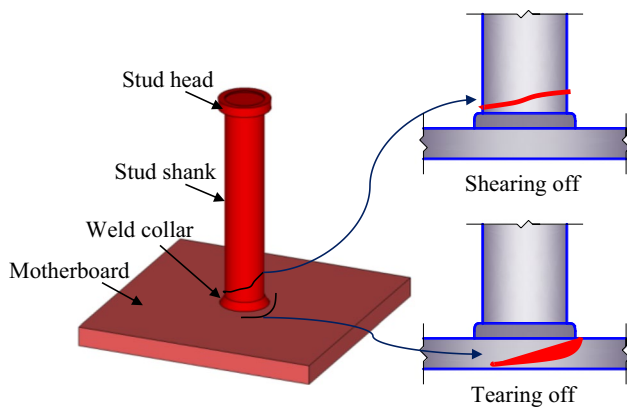


Fig. 2 Details and failure modes of studs

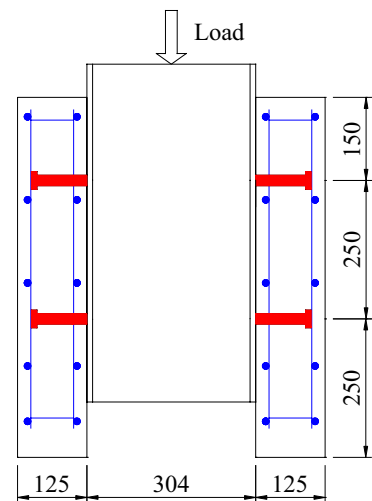
models are able to simulate the contact between studs and the concrete block. As a result, the local stress distribution at the root of studs, the stress of the surrounding concrete, and the stress concentration near the notches of weld toes are probably predicted. These local stresses near the root of studs usually govern the mechanical behaviors of studs, since studs may subject to plastic shear failure at the root in monolithic tests and fatigue failure initiated at weld toes of the stud shank and the beam in cyclic stress (Hanswille et al. 2007; Ovuoba and Prinz 2016), as shown in Fig. 2. It seems that the possible local stress concentration of studs considering concrete creep effects is of paramount importance. FEA with solid elements ought to be an effective way to investigate the local behavior of studs under long-term loads.

In this paper, the push-out specimen under constant shear force is carried out to study the creep effects on studs. The creep properties of concrete are considered using the rate of creep method (RCM), and the solid model is verified using previous test results. Through the local stress analysis of concrete, the influence of creep on the contact pressure of studs and concrete is determined and the stress concentration factor at the root of studs is obtained.

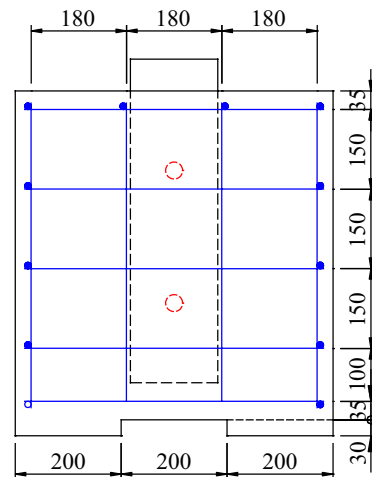
2 Details of Push-Out Specimen

Generally, push-out tests are regarded as sophisticated test methods to explore the mechanical behavior of studs, and are recommended by Eurocode 4 (2004) as the standard procedure. In this paper, the push-out specimen used by Al-deen et al. (2011) is analyzed using the solid model. The specimen follows the specifications suggested by Eurocode 4 (2004) and the test results are used to verify the solid model.

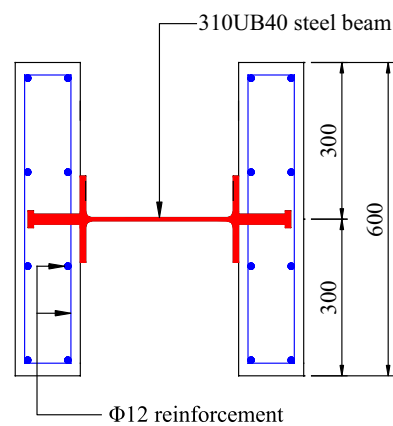
The geometric parameters of the specimen are shown in Fig. 3. The concrete slab width and thickness are 600 and 125 mm, respectively. Each slab is reinforced with 5 layers of 12 mm rebars. The steel web and the steel beam flange are



(a) Front view



(b) Side view



(c) Top view

Fig. 3 The geometry of push-out test specimen (unit: mm)

10.2 mm and 6.1 mm thick, respectively. Double studs with the center–center distance of 250 mm are arranged along the mid-line of each steel beam flange.

In composite bridges, the stud diameter is usually 19 and 22 mm. The length is about 100 to 250 mm. Previous researches showed that the length over 5 times of diameter had little influence on the elastic behavior of studs subjected to shear (Oehlers and Bradford 1999). In addition, to keep consistent with the long-term push-out test, the length of the stud is 100 mm and the diameter is 19 mm.

3 Finite Element Modeling

3.1 Finite Element Type, Mesh, Boundary Condition and Load

The solid element model considering concrete creep is built using the commercial software ANSYS10.0. Taking advantage of the symmetry, only half of the specimen is modeled, as shown in Fig. 4. The steel beam, studs, and concrete slabs are meshed with solid bricks Solid185, which has 8 nodes per element. The steel rebars are meshed with the beam element. The contact surfaces of the steel beam and studs are covered using Target170 and the contact surfaces of concrete slabs are covered using Conta174.

In order to capture the possible stress concentration of the stud connector, the global mesh size of the specimen is about 10 mm, while the local mesh size is about 1 mm.

According to the experimental constraints and the symmetry of the model, rigid restraints are applied to the bottom of the concrete slabs, and the symmetric constraints are imposed on the steel web.

For concrete structures in the state of serviceability, the working stress is mostly not more than 0.4 times of their compressive strength. In this case, the concrete can be regarded as a linear viscoelastic material, and the creep effect of concrete structures can be predicted by linear creep theory and superposition principle. Therefore, the linear

elastic constitutive of concrete is used, Young's modulus of concrete is 25.5×10^3 MPa and Poisson's ratio is 0.167.

Previous tests show that within the linear creep range, the creep Poisson's ratio is approximately constant with time and equal to the elastic Poisson's ratio, and the spatial creep of concrete is considered as isotropic (Jordaan and Illston 1969; Li 1994; Charpin et al. 2018). This simulation strategy has been proved to well predict the long-term evolution of concrete multiaxial creep (Sellier et al. 2016; Charpin et al. 2017). In this paper, the creep Poisson's ratio is 0.167.

For steel–concrete composite structures in normal service stage, the steel members are basically in the elastic stage, and the linear elastic constitutive of steel is used. Young's modulus of structural steel is 200×10^3 MPa and Poisson's ratio is 0.3. The material parameters are in accordance with the long-term test specimen.

The uniform pressure stress of 25.5 MPa was applied on the top cross-section of the steel beam to represent the 130 kN push out force. The applied force is about 30% of the ultimate load carrying capacity of the studs, and the shear-slip constitutive of the stud is linear under this load level (Oehlers and Bradford 1999). Thus, the elastic analysis of the push-out test is reasonable.

3.2 Creep Properties of Concrete

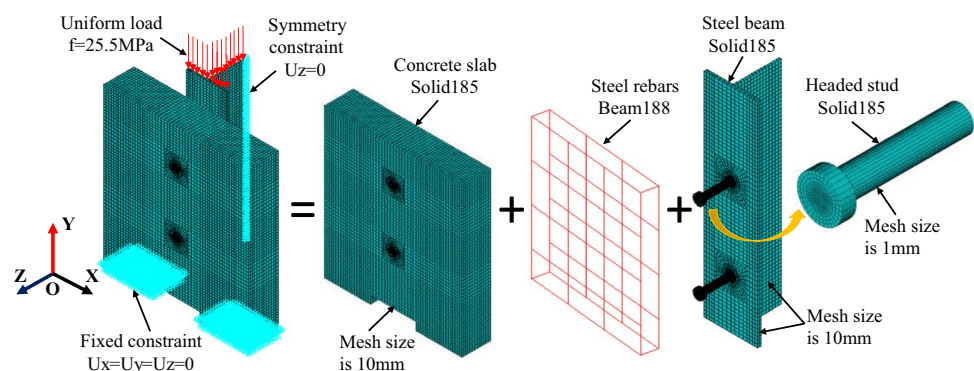
According to the *fib Mode Code* (2010), the creep coefficient φ with varying loading ages from 3 days, 7 days, 14 days, 90 days to 10 years are derived according to the test environment, as shown in Fig. 5.

According to the superposition law, the initial concrete stress $\sigma_c(t_0)$ is applied at time t_0 , with varying stress $\sigma_c(t)$ and time, the stress-dependent strain $\varepsilon_\sigma(t, t_0)$ of concrete can be expressed as Eq. (1) (Bažant and Wittmann, 1982).

$$\varepsilon_\sigma(t, t_0) = \frac{\sigma_c(t_0)}{E_c(t_0)} [1 + \varphi(t, t_0)] + \int_{t_0}^t \frac{\partial \sigma_c(\tau)}{\partial \tau} \cdot \frac{1 + \varphi(t, \tau)}{E_c(\tau)} d\tau \quad (1)$$

where $\varepsilon_\sigma(t, t_0)$ includes the elastic strain and creep strain. $E_c(\tau)$ is the elastic modulus of the concrete at time τ . $\varphi(t, \tau)$

Fig. 4 Mesh division and boundary constraint of FEM



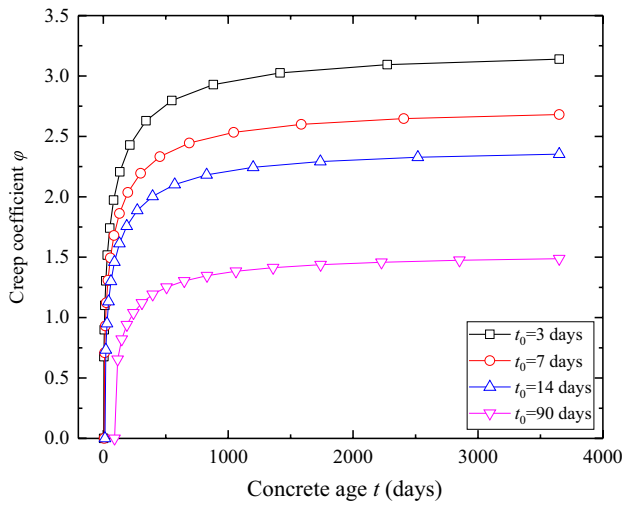


Fig. 5 Creep coefficient according to fib Mode Code (2010)

is the creep coefficient of concrete from time τ to t . t is the final time and τ is the loading time.

The continuous process can be divided into n segments, within a short time interval $\Delta t_n = t_n - t_{n-1}$, the creep strain increment of concrete $\Delta \varepsilon_{cr}(t_n, t_{n-1})$ is written as Eq. (2).

$$\Delta \varepsilon_{cr}(t_n, t_{n-1}) = \frac{\Delta \sigma_c(t_0)}{E_c(t_0)} [\varphi(t_n, t_0) - \varphi(t_{n-1}, t_0)] + \sum_{i=1}^{n-1} \frac{\Delta \sigma_c(t_i)}{E_c(t_i)} [\varphi(t_n, t_i) - \varphi(t_{n-1}, t_i)] \quad (2)$$

According to RCM (Gilbert and Ranzi 2011), the rate of creep is independent of loading age. Thus, the creep coefficient increment $\varphi(t_n, t_i) - \varphi(t_{n-1}, t_i) = \varphi(t_n, t_0) - \varphi(t_{n-1}, t_0)$. Assuming that Young’s modulus of concrete is constant, that is $E_c(t_i) = E_c(t_0)$, Eq. (2) can be revised to Eq. (3).

$$\Delta \varepsilon_{cr}(t_n, t_{n-1}) = \frac{\sigma_c(t_{n-1})}{E_c(t_0)} [\varphi(t_n, t_0) - \varphi(t_{n-1}, t_0)] \quad (3)$$

The material model CREEP provided by ANSYS specifies creep strain increment $\Delta \varepsilon_{cr}$ as Eq. (4) (Ansys Inc. 2010).

$$\Delta \varepsilon_{cr} = C_1 \sigma^{C_2} \varepsilon_{cr}^{C_3} e^{-C_4/T} \Delta t \quad (4)$$

where σ is equivalent stress. ε_{cr} is equivalent creep strain. T is temperature. $C_1 \sim C_4$ are constants. e is a natural logarithm base.

In this paper, the creep included only by stress variation is considered. Thus, $C_2 = 1$, $C_3 = C_4 = 0$. Given Eqs. (3) and (4) are compared, the creep constant C_1 can be expressed as Eq. (5).

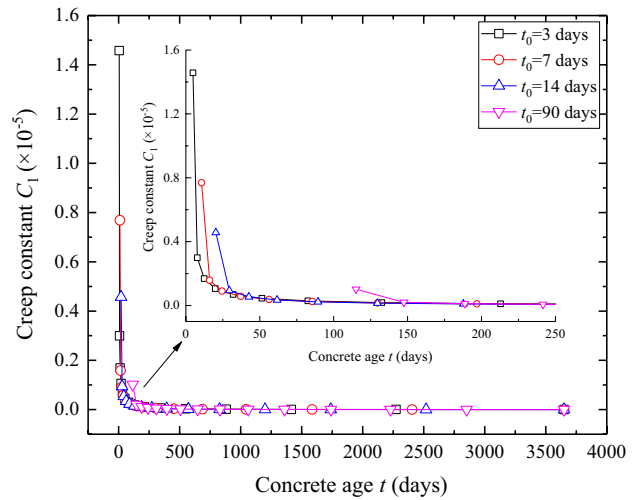


Fig. 6 Creep constant C_1 with different loading age

$$C_1 = \frac{\varphi(t_n, t_0) - \varphi(t_{n-1}, t_0)}{\Delta t_n} \frac{1}{E_c(t_0)} \quad (5)$$

According to the Eq. (5) and Fig. 5, the creep constant C_1 with various loading ages is shown in Fig. 6. The material properties of the CREEP model and creep constant C_1 are attributed to the slabs.

Although RCM is regarded as an out of date theory to predict concrete creep, especially when complex loading history of aged concrete is encountered. However, RCM can be easily connected with the CREEP material model provided by ANSYS. Besides, the FEA results show an acceptable approximation compared with the test results in the following verification. Thus, the RCM is used in this paper to evaluate creep effects of stud connectors.

3.3 Verification of FEM

To verify the solid model under short-term load, slip deformation by FEA is compared with previous test results (Nguyen and Kim 2009; Okada et al. 2006; Wang 2013). All solid models are built according to the specific detail of each test. The friction coefficient of the steel–concrete interface is taken as 0 and 0.25, respectively, including beam-concrete friction coefficient u_1 and stud-concrete friction coefficient u_2 , as shown in Fig. 7 (Guezouli and Lachal 2012). The relative error of slip under three cases is calculated respectively, as shown in Fig. 8. When the stud-concrete friction is not considered, the FEA results are higher than the test results, and the relative errors of the slip in the three push-out tests are all more than 5%. After considering the stud-concrete friction, the absolute relative errors of the slip in three push-out tests are all within 5%. However, the influence of

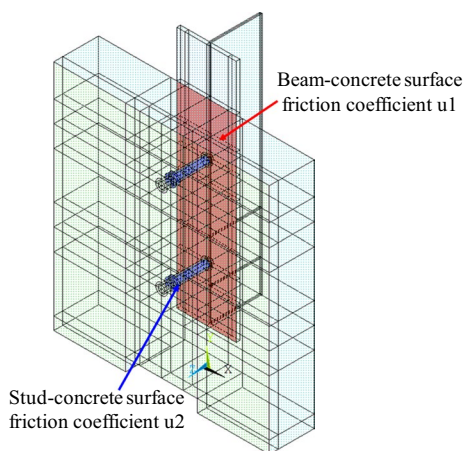


Fig. 7 Contact surfaces of the finite element model

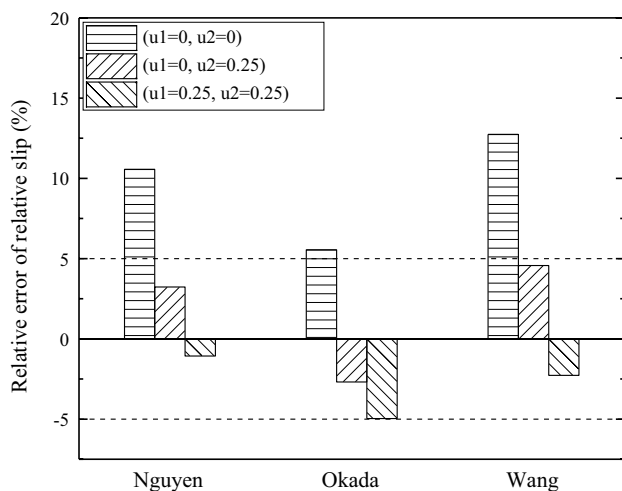


Fig. 8 Verification of FEM under the short-term load

beam-concrete friction on the model accuracy cannot be determined qualitatively according to the short-term test results. Due to the fact that the steel flange is greased to reduce the bonding and friction in the actual push-out test, the friction coefficient u_1 of the beam-concrete interface is assumed to be zero. Therefore, the friction coefficient of FEM is $u_1 = 0$ and $u_2 = 0.25$ in this paper.

The relative slip of the steel-concrete interface by FEA is compared with the result of the long-term push-out test reported by Al-deen et al. (2011), as shown in Fig. 9. Three verification strategies are adopted here, labeled as strategy 1, strategy 2 and strategy 3, respectively. In strategy 1, the load level is determined according to the initial relative slip, and the creep coefficient of the age at initial loading obtained from the test is approximated by the *fib* model. Strategy 2 differs from strategy 1 in that the creep properties of concrete are derived from the final value of long-term relative slip. Strategy 3 is

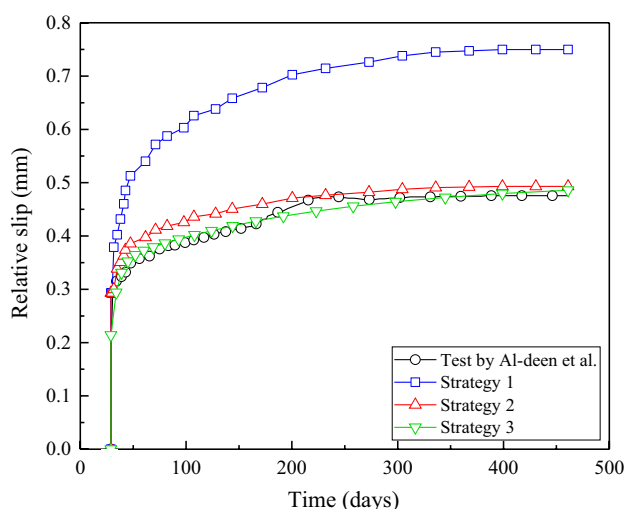


Fig. 9 Verification of FEM under the long-term load

that the creep coefficient curve of the test is adopted to represent the creep properties of concrete, the initial relative slip is calculated from the final long-term relative slip, and the load level is determined correspondingly. After comparison, the prediction accuracy of strategy 3 is the highest among the three strategies, and its calculation results can reflect the long-term performance of headed stud connectors.

Therefore, strategy 3 is adopted in this paper. Under this condition, the absolute relative error of the final long-term slip is within 3%. It seems that the solid model using RCM is close to the test results under long-term load. RCM is used in this paper to study the stress redistribution of studs under constant shear force.

4 Results and Discussion

4.1 Stress of Concrete

4.1.1 Bearing Stress Analysis

It can be observed from previous push-out tests (Xu et al. 2012; Yang et al. 2018) that at the ultimate load stage, the concrete surrounding stud root may subject to local crush, owing to local stress concentration.

To evaluate the stress concentration and stress distribution of the surrounding concrete considering concrete creep effects, local bearing stress of concrete is analyzed. The stress concentration factor (SCF) K_{cy} is defined as Eqs. (6) and (6a).

$$K_{cy} = \frac{\sigma_{cy}}{\sigma_{y0}} \tag{6}$$

$$\sigma_{y0} = \frac{V_0}{h_s D_s} \tag{6a}$$

where σ_{cy} is the y-axial stress of concrete, and σ_{y0} is the averaged y-axial stress. V_0 is the shear force per stud, $V_0 = 32.5\text{kN}$. D_s is the diameter of stud, $D_s = 19\text{ mm}$. h_s is the height of studs, $h_s = 100\text{ mm}$.

Given the loading age $t_0 = 7$ days and $t = 10$ years, the bearing the SCF contours of concrete at $t = t_0$ and $t = 10$ years are shown in Fig. 10. The bearing the SCF distribution of concrete along the stud shank is shown in Fig. 11a. Under short-term load, the bearing stress of concrete is relatively concentrated within the range of $2D_s$ along the stud shank direction, and SCF at the root of the stud reaches its peak with K_{cy} is about 5.8. Previous researches by Utescher (1978) and Shao (2015), assumed that the distribution of the y-axial bearing stress of concrete is triangular along the shank and the stress concentration range is about $1.7D_s$ and the peak K_{cy} is about 6. An analytical prediction maximum bearing stress is expressed as Eq. (7), where $h = 1.7D_s$. Under the short-term load, σ_{\max} using FEA is about 3.3% lower than the analytical result. It seems that the equation is a reasonable approximation of the stress peak.

$$\sigma_{\max} = \frac{2.5V_0}{h \times 1.15D_s} \quad (7)$$

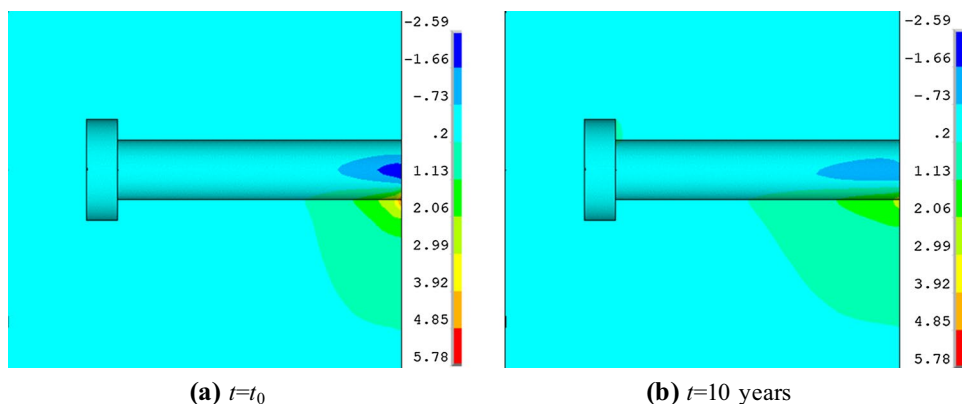
Given the concrete age $t = 30$ days, the Y-axial bearing stress of the surrounding concrete decreases at the root of the stud and increases near the weld toe along the stud shank direction. Compared with the short-term results, the SCF of the surrounding concrete decreases by nearly 27%, while the distribution height of bearing stress increases by almost 25% along the stud shank, and the distance between the center of the bearing force and the root of the stud increases by 48.6%. When the concrete age $t = 10$ years, compared with the initial loading stage, the SCF of the surrounding concrete decreases by about 52% at the root of the stud, while the distribution height of the bearing stress increases by almost 50%, and the distance between

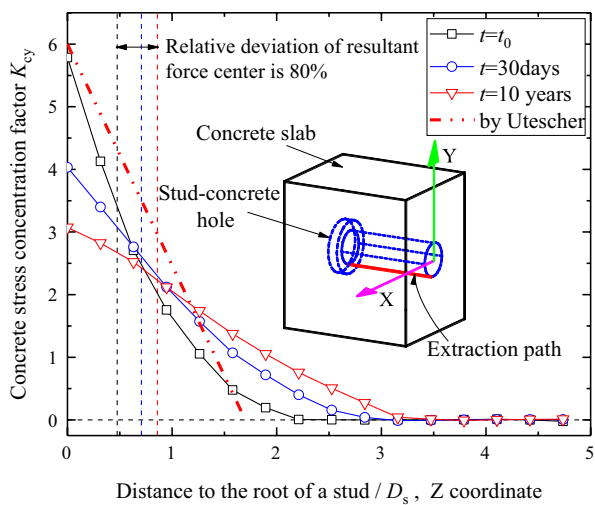
the center of the bearing force and the root of the stud increases by nearly 80%.

It can be seen that the shear force at the root of the stud is mainly borne by the local concrete near the stud foot, and the bearing stress concentration appears in the surrounding concrete at the root of the stud. As the loading time increases, the confined concrete undergoes creep deformation, the peak stress of concrete decreases at the root of the stud, and the distribution height of the bearing stress increases along the stud shank. The stress redistribution of the surrounding concrete appears along the stud shank direction, that is, the surrounding concrete is unloaded at the root of the stud and loaded near the weld toe. Creep is beneficial to the long-term bearing pressure of the surrounding concrete. However, after the long-term load, the reaction center of the surrounding concrete on the stud is far away from the root of the stud, and the resultant reaction force changes little. The additional bending moment at the root of the stud is increased by the surrounding concrete, leading to the bending deformation of the stud increases, which results in the relative slip of the steel–concrete interface increasing, thus reducing the composite behavior between steel and concrete.

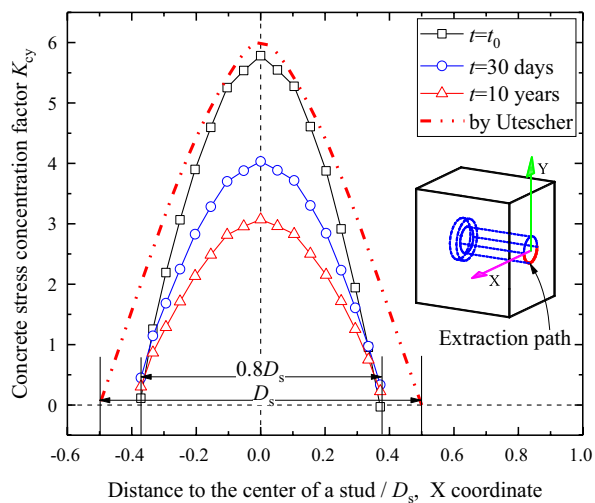
In order to analyze the distribution of bearing stress along the diameter of the concrete hole (x direction), the y-axial bearing stress is extracted along the lower edge of the concrete hole at the root of the stud, the results at different concrete ages are shown in Fig. 11b. The horizontal axis represents the ratio of the x-direction distance to the center of the concrete hole to the diameter D_s of studs, and the vertical axis represents the SCF of the surrounding concrete K_{cy} . Under the short-term load, the distribution of the bearing stress in the surrounding concrete is approximately parabolic along the transverse direction, and the peak stress appears at the lower edge of the concrete hole ($x = 0$). The SCF of the surrounding concrete $K_{cy} = 5.8$ and the width of the transverse distribution is about $0.8D_s$. Utescher assumed that the distribution of bearing stress in the surrounding concrete is parabolic in the transverse direction and the distribution width of the bearing stress is $1.0D_s$ under the short-term

Fig. 10 Bearing the SCF contours of concrete

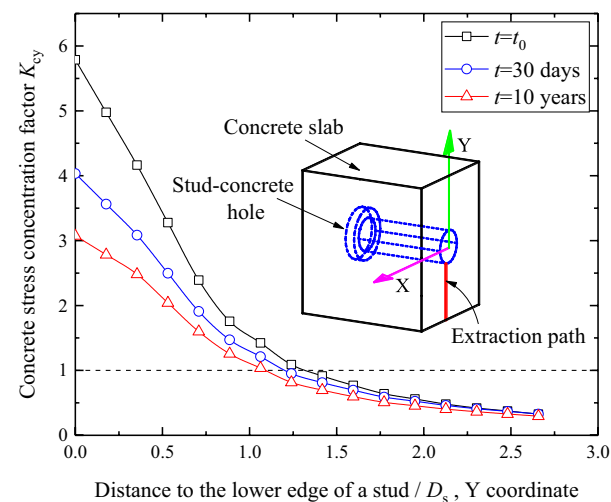




(a) Distribution along the stud shank



(b) Distribution along the concrete hole



(c) Vertical distribution

Fig. 11 Bearing stress of surrounding concrete

load. Compared with the FEA results obtained in this part, the distribution shape of bearing stress assumed by Utescher (1978) is reasonable, but the distribution width of the bearing stress needs to be further modified. As the loading time increases, the concrete creep deformation causes the peak bearing stress to decrease, while the transverse distribution width remains substantially unchanged. Compared with the short-term load, the peak bearing stress of concrete decreases by almost 31% at age $t=30$ days and 46.6% at age $t=10$ years, respectively. The results show that under the long-term effect, the distribution width of bearing stress is basically unchanged along the transverse direction, while the surrounding concrete appears to be unloaded significantly at the root of the stud. Combined with the results in Fig. 11a, it can be seen that the bearing stress of the surrounding concrete is redistributed along the stud shank direction.

When the stud shear connector is damaged, the concrete under its root tends to appear local crushing. In order to analyze the influence of the long-term load on the transmission and distribution of concrete bearing stress under the stud, the distribution of concrete bearing stress at different ages is extracted along the height of the concrete slab, as shown in Fig. 11c. The horizontal axis is the ratio of the y-direction distance to the lower edge of the stud to the diameter D_s , and the vertical axis is the SCF of concrete K_{cy} . Under the short-term load, the bearing stress concentration appears in the concrete within nearly $1.0D_s$ from the lower edge of the stud, and the bearing stress decreases linearly along the height of the concrete slab, while the bearing stress tends to be stable beyond the height of $1.0D_s$. With the increase of loading time, the bearing stress concentration decreases at the lower edge of the concrete hole, and the distribution trend of bearing stress along the height direction is similar to the short-term condition. Compared with the short-term results, the peak bearing stress at the lower edge of the concrete hole decreases by 31% at the concrete age $t=30$ days and 47% at the concrete age $t=10$ years, respectively. Under the short-term and long-term loading conditions, the bearing stress concentration appears in concrete within the height of $1.0D_s$ from the lower edge of the stud, and the creep reduces the peak bearing stress of concrete, which is beneficial to the bearing pressure of concrete. However, the compressive strain generated by the local bearing stress accumulates in the height direction, resulting in large deformation, thereby leading to an increase in the relative slip of the steel–concrete interface, and the long-term deformation of the surrounding concrete cannot be ignored. The stud connector is simply simulated by the beam element or the spring element, which cannot capture the local bearing stress concentration around the stud, indicating that the solid model has great advantages in analyzing the local effect of the stud connector.

4.1.2 Splitting Stress Analysis

In addition to the vertical bearing stress, the concrete at the root of the stud is subjected to the splitting stress along the transverse direction. When the splitting tensile stress exceeds the tensile strength of concrete, vertical cracks will appear in the concrete, affecting the serviceability state of structures.

The splitting the SCF contours of concrete at $t = t_0$ and $t = 10$ years are shown in Fig. 12. The splitting stress at the lower edge of the stud is extracted along the transverse direction, and the results at different ages are shown in Fig. 13a. The splitting stress concentration factor K_{cx} is introduced to evaluate the concentration degree of the splitting stress, and the calculation of K_{cx} is shown in Eqs. (8)–(8b).

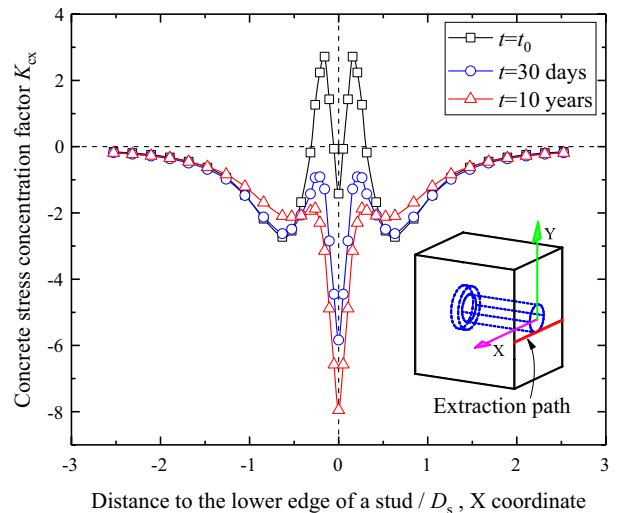
$$K_{cx} = \frac{\sigma_{cx}}{\sigma_{x0}} \tag{8}$$

$$\sigma_{x0} = \frac{2P_t}{h_s D_s} \tag{8a}$$

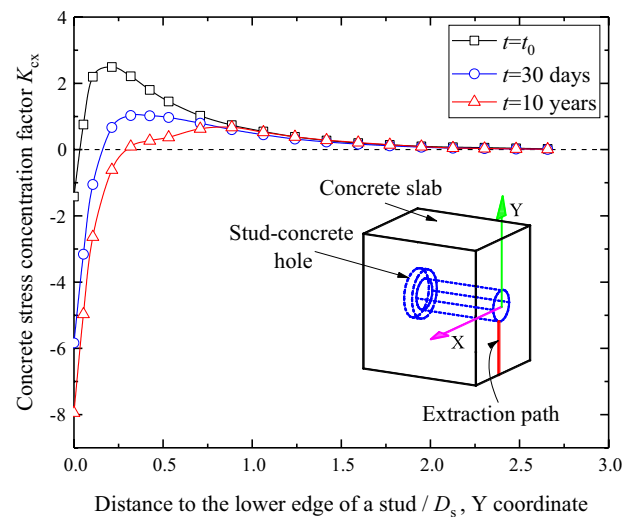
$$P_t = \frac{P_L (1 - D_s/b_c)^2}{\pi} \tag{8b}$$

where σ_{cx} is the x-axial splitting stress of concrete. σ_{x0} is the x-axial mean splitting stress. P_t is the equivalent splitting tensile force, calculated according to Eq. (8b) provided by Leonhard (1964). P_L is the equivalent pressure, $P_L = V_0$. b_c is the effective width of the concrete slab, here takes $b_c = 4D_s$. The remaining symbols have the same meanings and values as mentioned above.

At the beginning of creep, the compressive stress appears at the lower edge of the stud, and there is a splitting tension zone nearby. The K_{cx} of the peak tensile SCF is 2.72. The further away from the concentrated load, the compressive stress of concrete increases first and then decreases slowly to disappear along the transverse direction. With the increase of creep time, the splitting stress of concrete varies



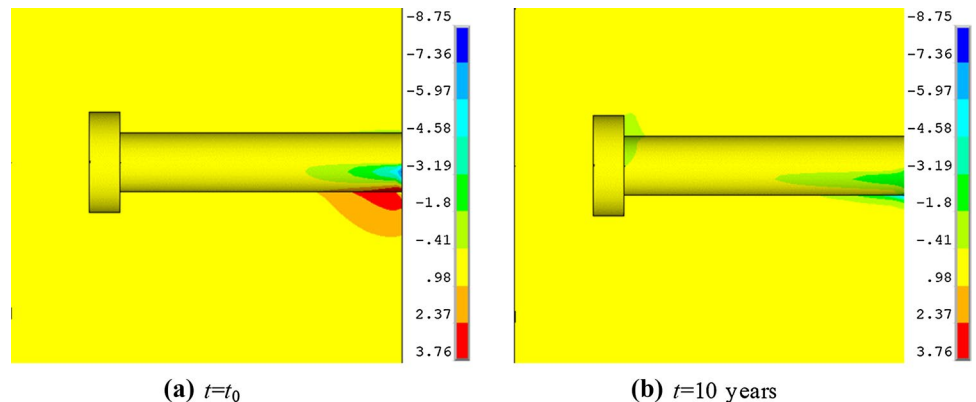
(a) Transverse distribution



(b) Vertical distribution

Fig. 13 Splitting stress of surrounding concrete

Fig. 12 Splitting the SCF contours of concrete



significantly in the range of $1.0D_s$ centered on the concrete hole. The peak compressive stress of the stud increases significantly, while the stress in the original splitting tension zone decreases and becomes compressive. The creep prevents the surrounding concrete from splitting tension along the transverse direction, which is beneficial to the stress of the surrounding concrete.

The vertical distribution of the concrete splitting stress is shown in Fig. 13b. The horizontal axis is the ratio of y-direction distance to the lower edge of the stud to D_s , and the vertical axis is the SCF of the concrete splitting stress K_{cx} . At the beginning of creep, the splitting stress of concrete changes from compression to tension and increases to the peak value. With the increase of vertical height to the lower edge of the stud, the splitting tensile stress of concrete decreases slowly and finally approaches zero at the height of $2.0D_s$. Under the long-term condition, the peak tensile stress of concrete decreases significantly. When the concrete age $t=30$ days, $K_{cx}=1.03$, which is almost 41% of that under the short-term load. When the concrete age $t=10$ years, $K_{cx}=0.67$, which is nearly 27% of that under the short-term load. The height of splitting tension zone also decreases with the increase of loading time.

It can be seen that creep is beneficial to the long-term stress of concrete. However, the peak splitting tensile stress of concrete is maximum under the short-term condition, while the early strength of concrete is relatively small, it is easy to appear splitting cracks, the early cracking of concrete cannot be ignored. In practical engineering, the reinforcement ratio should be increased around studs to prevent early cracking of concrete.

4.2 Stress of Steel Beam

The stud connector appears the stress concentration at the joint between the stud and steel beam due to resistance to the relative slip of steel–concrete interface. Under the repeated action of the live load, the steel beam is prone to fatigue damage at the weld toe. Previous studies on the fatigue performance of studs show that fatigue cracks are

easy to appear in the heat-affected zone of steel beam near the weld toe. When cracks grow and run through, the stud is prone to the fatigue failure mode that the motherboard is torn off. It is necessary to analyze the stress distribution of the steel beam at the stud to evaluate the fatigue performance of studs under the long-term service condition.

The y-axial stress concentration factor K_{by} of steel beam is introduced, and its calculation is shown in Eq. (9) and Eq. (9a).

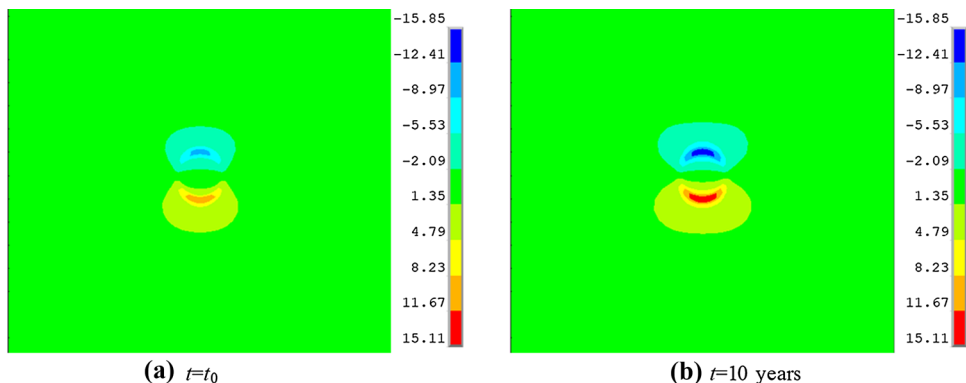
$$K_{by} = \frac{\sigma_{by}}{\sigma_{by0}} \tag{9}$$

$$\sigma_{by0} = \frac{P}{A_b} \tag{9a}$$

where σ_{by} is the y-axial stress of the steel beam. σ_{by0} is the y-axial mean stress of steel beam. P is the external force applied to the top of the steel beam, $P=130\text{kN}$. A_b is the cross-sectional area of steel beam, $A_b=5095.96\text{ mm}^2$.

The Y-axial the SCF contours of steel flange at $t=t_0$ and $t=10$ years are shown in Fig. 14. A transverse (X direction) path is made at the lower edge of the stud root, the Y-axial stress distribution of steel beam on this path is analyzed, as shown in Fig. 15a. The horizontal axis represents the ratio of distance to the stud center to the thickness b_s of steel flange along the x-axis, and the vertical axis represents the y-axial stress concentration factor K_{by} of the steel beam. Under the short-term load, the peak tensile stress appears in the steel beam at the lower edge of the stud, the tensile stress concentration appears within the range of about $3.0b_s$ from the stud center, and the SCF $K_{by}=8.7$. As the loading time increases, the peak tensile stress of steel beam increases significantly at the lower edge of the stud, while the distribution range of tensile stress does not change too much. The peak tensile stress increases by 22.8% at the concrete age $t=30$ days, and increases by 48.3% at $t=10$ years compared with that at the initial loading stage of concrete. The stress concentration effect of steel beam increases with the loading time at

Fig. 14 Y-axial the SCF contours of steel flange



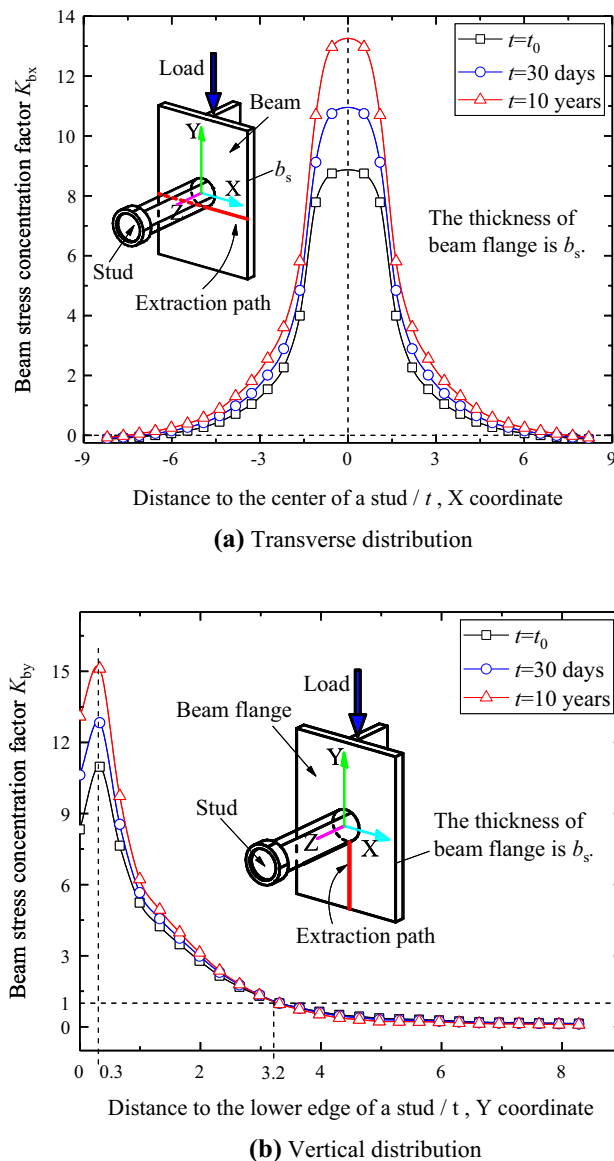


Fig. 15 Y-axial stress of steel flange

the lower edge of the stud, which is adverse for the stress of the steel beam.

Previous studies on the fatigue performance of studs (Hanswille et al. 2007) and the European code (CEN 2004) have shown that fatigue cracks of steel beam at the lower edge of the stud is perpendicular to the tensile stress direction, and it is reasonable to use the tensile stress of steel beam at the lower edge of the stud to evaluate the fatigue performance of the motherboard. In addition, it can be seen from Fig. 15a that the stress of steel beam near the stud increases with the loading time, and the long-term load of the push-out specimen is constant, the results of evaluating the fatigue performance of studs do not change according to the nominal stress $\sigma_s = V_0/A_s$ in the current

codes, where V_0 is the shear force per stud and A_s is the cross-sectional area of the stud. Therefore, the nominal stress of codes cannot evaluate the long-term fatigue performance of steel beam at the stud. It is advisable to establish a solid model and analyze the local stress state of steel beam at the stud with the creep calculation method of RCM to evaluate the long-term fatigue performance and safety of this component.

In order to determine the distribution range of the stress concentration effect of the steel beam at the stud, the y-axial stress is extracted along the height of the steel beam, as shown in Fig. 15b. The horizontal axis represents the ratio of y-direction distance to the lower edge of the stud to the thickness b_s of steel flange, and the vertical axis represents the y-axial stress concentration factor K_{by} of the steel beam. Under the short-term load, as the distance from the lower edge of the stud increases, the tensile stress of steel beam increases rapidly, and reaches its peak value at $0.3b_s$ from the lower edge of the stud, the SCF of tensile stress K_{by} is nearly 11, then it decreases to zero slowly. The tensile stress of the steel beam is concentrated within the range of $3.2b_s$ from the lower edge of the stud. As the loading time increases, the peak tensile stress of steel beam increases, while the peak position and the distribution range of tensile stress concentration remain basically unchanged. Compared with the short-term results, the SCF increases by 18% at the concrete age $t=30$ days, and increases by almost 36% at $t=10$ years. Long-term loading results in a significant increase in the tensile stress near the lower edge of the stud, which has a negative impact on the stress of the steel beam. According to the standard push-out test, the vertical spacing between studs is 250 mm, which is far beyond the stress concentration range. Therefore, the stress concentration area near the two studs does not affect each other, it is feasible to study the stress variation of steel beam near a single stud to predict that of other studs.

Due to the Poisson's effect, the y-axial and the x-axial strain are usually measured in the actual tests to obtain the biaxial stress state of the steel beam. In order to evaluate the biaxial stress variation of steel beam near the weld toe, the transverse stress σ_{bx} is analyzed. The x-axial stress concentration factor K_{bx} of steel beam is introduced, and its calculation is shown in Eq. (10).

$$K_{bx} = \frac{\sigma_{bx}}{\sigma_{by0}} \quad (10)$$

where σ_{bx} is the x-axial stress of the steel beam. σ_{by0} is the nominal mean y-axial stress of steel beam, and its calculation is shown in Eq. 9a.

The x-axial the SCF contours of steel flange at $t=t_0$ and $t=10$ years are shown in Fig. 16. The x-axial stress is

Fig. 16 X-axial the SCF contours of steel flange

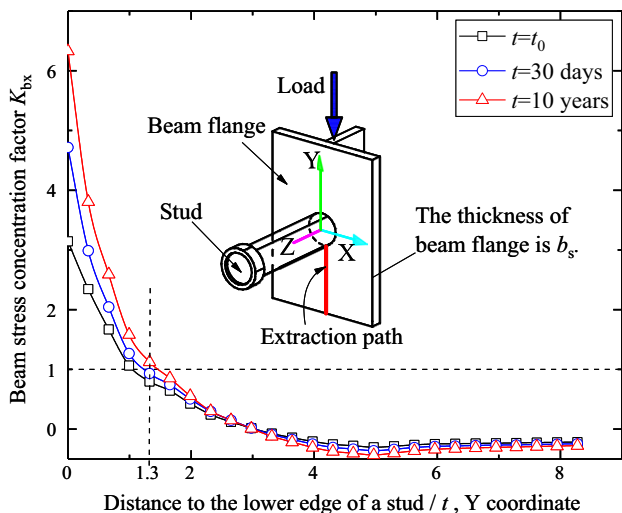
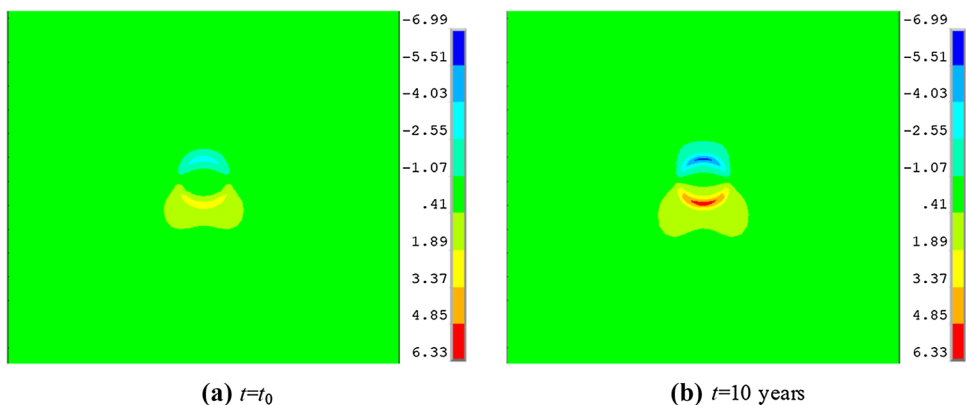


Fig. 17 X-axial stress of steel flange, vertical distribution

extracted along the height of the steel beam, as shown in Fig. 17. At the initial loading stage, the peak tensile stress of the steel beam appears at the lower edge of the stud. As the distance from the lower edge of the stud increases, the tensile stress of steel beam decreases to disappear gradually. The x-axial tensile stress concentration appears in the steel beam within the range of $1.3b_s$ from the lower edge of the stud. As the loading time increases, the tensile stress of steel beam increases significantly in the range of $1.3b_s$ from the lower edge of the stud, while the x-axial stress of steel beam is substantially the same outside this range. When the concrete age $t=30$ days, the x-axial peak stress of steel beam $K_{bx}=4.7$, which is 51.6% higher than that under the short-term condition. When the concrete age $t=10$ years, the x-axial peak stress of steel beam $K_{bx}=6.3$, which is about 1.1 times higher than that under the short-term condition. The stress concentration of steel beam near the weld toe is aggravated by concrete creep. The effect generated by the superposition of the tensile stress increment caused by concrete creep, the residual tensile

stress in the welding process, and the repeated action of live load, are unfavorable to the fatigue stress of steel members.

4.3 Stress of Stud

4.3.1 Bending Stress Analysis

Previous studies on the push-out tests show that the failure mode of studs is mainly bending-shear failure at its root. The bending stress at the root of the stud is closely related to its stress state. In addition, the fatigue test studies show that the stud may have fatigue cracks at the weld toe. It is necessary to analyze the bending stress concentration on the surface of the stud near the weld toe and the influence of long-term loading on the stress distribution.

In addition to the vertical shear force transmitted by the steel beam, the deformation at the root of the stud is restrained by the steel beam flange and produces bending moment, resulting in the tension stress at the lower edge of the stud. The bending stress concentration factor K_{sb} of studs is calculated as shown in Eqs. (11) and (11a).

$$K_{sb} = \frac{\sigma_{sb}}{\sigma_{sb0}} \tag{11}$$

$$\sigma_{sb0} = \frac{M_0}{I_s} \cdot \frac{D_s}{2} \tag{11a}$$

where σ_{sb} is the Z-axial bending stress of studs. σ_{sb0} is the z-axial mean bending stress of studs. M_0 is the moment at the root of a stud, calculated by FEM under the short-term condition, $M_0=157996$ N·mm. I_s is the inertia moment of the stud section, $I_s=6397$ mm⁴. D_s is the diameter of the stud, $D_s=19$ mm.

The bending the SCF contours of the stud at $t=t_0$ and $t=10$ years are shown in Fig. 18. Figure 19 shows the distribution of bending stress along the stud shank (z direction) at the lower edge of the stud. At the initial loading stage,

Fig. 18 Bending the SCF contours of the stud

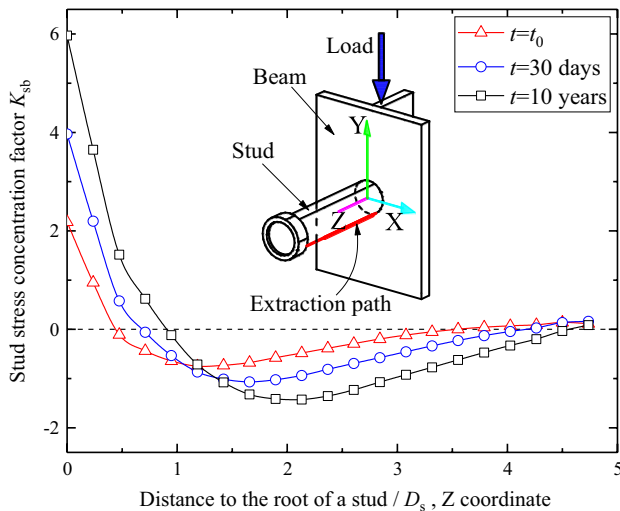
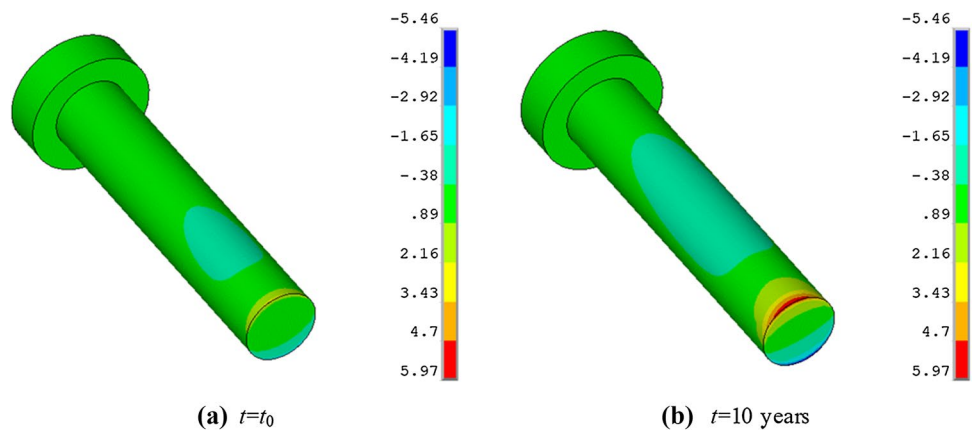


Fig. 19 Bending stress distribution of the stud

the peak tensile stress appears at the root of the stud, and the SCF of tensile stress $K_{sb} = 2$. The bending stress reduces gradually as the distance from the root of the stud increases, and its distribution height is about $0.4D_s$ along the stud shank. Beyond this range, the bending compressive stress appears in the cross-section of the stud. Along the height of stud shank, the bending compressive stress increases first, reaches its peak value near $1.0D_s$, and then gradually decreases to disappear. As the loading time increases, the peak bending tensile stress and the distribution height of tensile stress increases significantly. When the concrete age $t = 30$ days, the SCF $K_{sb} = 4.0$ at the root of the stud, which is about twice as high as that under the short-term condition. The distribution height of tensile stress is about $0.5D_s$, which is 25% higher than the short-term results. When the concrete age $t = 10$ years, the SCF $K_{sb} = 6.0$ at the root of the stud, which is about 3 times as high as that under the short-term condition, and the distribution height of tensile stress is nearly $0.9D_s$, which is 1.25 times higher than the short-term

results. Outside this range, the compressive stress of the stud increases with the loading time, and the peak position of compressive stress is also far away from the root of the stud.

The creep deformation of the surrounding concrete is equivalent to the reduction of bearing stiffness on the stud. During the entire long-term loading process, the stud shank is always in close contact with the bearing concrete, causing the deformation of the stud to increase. The reaction moment at the root of the stud restrained by the steel flange plate increases correspondingly, resulting in the increase of bending stress in the stud section. For stud shear connectors with the bending-shear failure as the main failure mode, the stress concentration at the root of the stud becomes more significant and the stud suffers the time-varying damage after the long-term loading. In addition, weld defects and residual stresses are inevitable in the welding process, and the stress concentration effect caused by the long-term loading accelerates the development of weld defects, thereby reducing the bearing capacity of stud connectors.

4.3.2 Shear Stress Analysis

Under the action of vertical concentrated shear force, the shear failure is prone to appear at the root of the stud. In order to study the effect of long-term loading on the shear behavior of studs, the SCF of the stud K_{ss} is introduced, as shown in Eqs. (12) and (12a).

$$K_{ss} = \frac{\tau_{ss}}{\tau_{ss0}} \tag{12}$$

$$\tau_{ss0} = \frac{V_0}{A_s} \tag{12a}$$

where τ_{ss} is the shear stress at the lower edge of the studs. τ_{ss0} is the nominal shear stress of studs. A_s is the cross-sectional area at the root of a stud and V_0 is the applied shear force at the root of a stud.

Fig. 20 Shear the SCF contours of the stud

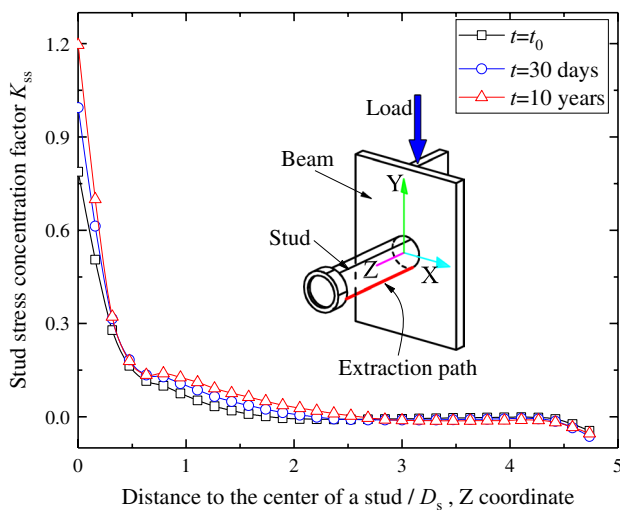
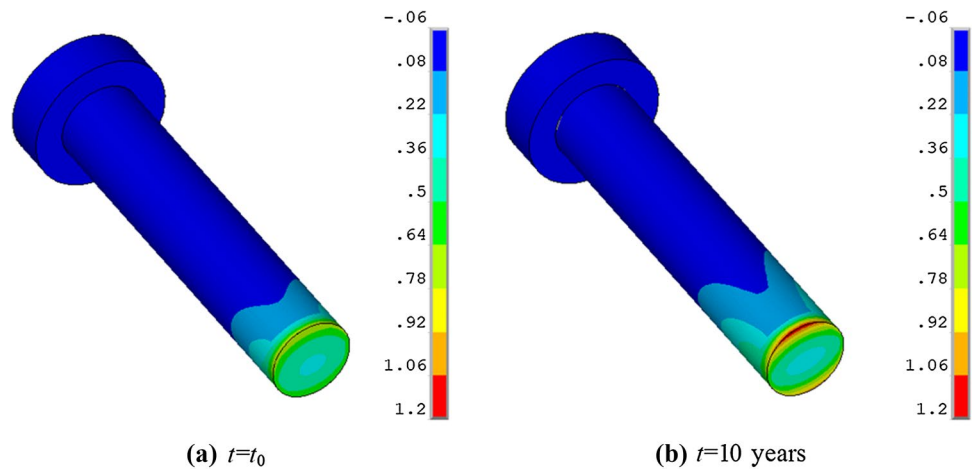


Fig. 21 Shear stress distribution of the stud

The shear the SCF contours of the stud at $t = t_0$ and $t = 10$ years are shown in Fig. 20. The vertical shear stress (the shear plane is XY plane and the direction is along the y-axis) at the lower edge of the stud is analyzed, as shown in Fig. 21. At the initial loading stage, the peak shear stress appears at the root of studs, and the SCF is almost 0.8. Along the stud shank direction, the shear stress decreases to disappear gradually. As the loading time increases, the peak shear stress increases, as the distance from the root of studs increases, the variation of shear stress at the lower edge of the stud is small. When the concrete age $t = 20$ days, the peak shear stress K_{ss} at the root of the stud is 1.0, which is 26.6% higher than the short-term results. When the concrete age $t = 10$ years, the peak shear stress K_{ss} is 1.2, which is almost 52% higher than the short-term results. It can be seen that the peak shear stress appears at the upper and lower edges of the stud root due to the influence of boundaries restrained by the steel flange plate. The shear stress concentration of the

stud is aggravated significantly owing to the concrete creep effect, which has a negative effect on the long-term shear behavior of studs.

5 Conclusions

The solid finite element model of the push-out test with headed studs is established, the creep algorithm of RCM is used to consider the creep properties of concrete. The local stresses of the concrete slab, steel beam and studs are analyzed, and the following conclusions are obtained:

- (1) The solid model can truly reflect the local stress state of the stud and the surrounding concrete. Combined with the creep algorithm of RCM, the predicted short-term and long-term relative slip at the steel–concrete interface is close to the test results, and the relative error is less than 3%, indicating that the creep effects prediction of the solid model is reliable.
- (2) Compared with the short-term results, the peak bearing stress of the surrounding concrete decreases by 52%, and the distribution height along the stud shank increases by 50% after 10 years of creep. The stress redistribution appears along the stud shank that the surrounding concrete is unloaded at the root of studs and loaded near the weld toe. The creep effect is beneficial to the long-term stress of concrete. However, the distance between the center of bearing resultant force and the root of studs increases by 80.7%, the reaction moment increases at the root of studs, the bending deformation of studs increases correspondingly, resulting in the increase of relative slip in the steel–concrete interface, thus reducing the composite behavior of steel and concrete under the long-term loading.
- (3) Compared with the short-term condition, the bending tensile stress and shear stress at the root of studs

increases by two times and nearly 52% respectively after 10 years of creep. The time-varying damage of studs appears due to the significant stress concentration at the root of studs, which is unfavorable to the long-term shear and fatigue performance of studs.

Acknowledgements The research reported herein has been carried out as part of the research project granted by the National Natural Science Foundation of China (51978245). This paper is also partly supported by the Fundamental Research Funds for National Universities (2019B13314). The assistances are gratefully acknowledged.

References

- Al-deen, S., Ranzi, G., & Vrcelj, Z. (2011). Full-scale long-term experiments of simply supported composite beams with solid slabs. *Journal of Constructional Steel Research*, 67, 308–321.
- Ansys Inc. (2010). Material reference. Chapter 3.5.5: Creep, Canonsburg.
- Ban, H., Uy, B., Pathirana, S. W., Henderson, I., Mirza, O., & Zhu, X. (2015). Time-dependent behaviour of composite beams with blind bolts under sustained loads. *Journal of Constructional Steel Research*, 112, 196–207.
- Bažant, Z. P., & Wittmann, F. H. (1982). *Creep and Shrinkage in Concrete Structures*. New York: Wiley.
- Bonilla, J., Bezerra, L. M., & Mirambell, E. (2019). Resistance of stud shear connectors in composite beams using profiled steel sheeting. *Engineering Structures*, 187, 478–489.
- Charpin, L., Le Pape, Y., Coustabeau, É., Toppani, É., Heinfing, G., Le Bellego, C., et al. (2018). A 12 year EDF study of concrete creep under uniaxial and biaxial loading. *Cement and Concrete Research*, 103, 140–159.
- Charpin, L., Sow, T. O., D'Estève de Pradel, X., Hamon, F., & Mathieu, J.-P. (2017). Numerical simulation of 12 years long biaxial creep tests: Efficiency of assuming a constant Poisson's ratio. *Poromechanics*, 6, 997–1004.
- European Committee for Standardization (CEN). (2004). *Eurocode 4: Design of composite steel and concrete structures—Part 1.1: General rules and rules for buildings*. Brussels, EN 1994-1-1.
- fédération internationale du béton (fib). (2010). *Model Code 2010: First draft* (Vol. 1). London.
- Gilbert, R. I., & Ranzi, G. (2011). *Time-dependent Behavior of Concrete Structures*. London: Taylor & Francis Group.
- Guezouli, S., & Lachal, A. (2012). Numerical analysis of frictional contact effects in push-out tests. *Engineering Structures*, 40, 39–50.
- Guezouli, S., Lachal, A., & Nguyen, Q. H. (2013). Numerical investigation of internal force transfer mechanism in push-out tests. *Engineering Structures*, 52, 140–152.
- Han, Q., Wang, Y., Xu, J., Xing, Y., & Yang, G. (2017). Numerical analysis on shear stud in push-out test with crumb rubber concrete. *Journal of Constructional Steel Research*, 130, 148–158.
- Hanswille, G., Porsch, M., & Ustundag, C. (2007). Resistance of headed studs subjected to fatigue loading part II: Analytical study. *Journal of Constructional Steel Research*, 63, 485–493.
- Huang, D., Wei, J., Liu, X., Du, Y., & Zhang, S. (2019). Experimental study on influence of post-pouring joint on long-term performance of steel-concrete composite beam. *Engineering Structures*, 186, 121–130.
- Japan Road Association (JRA). (2002). *The instruction of railway bridge construction and commentary. Part 2: Steel bridge*. Tokyo. (In Japanese).
- Jordaan, I. J., & Illston, J. M. (1969). The creep of sealed concrete under multiaxial compressive stresses. *Magazine of Concrete Research*, 21(69), 195–204.
- Leonhardt, F. (1964). *Prestressed concrete: design and construction* (2nd ed.). Berlin-Wilmersdorf: Wilhelm Ernst & Sohn.
- Li, Z. (1994). Effective creep Poisson's ratio for damaged concrete. *International Journal of Fracture*, 66(2), 189–196.
- Liu, Y. Q., Chen, C., & Zheng, S. J. (2015). Analysis of force mechanism of pylon anchorage structure of fixed-end steel anchor box type. *Bridge Construction*, 45(1), 33–38. (In Chinese).
- Liu, R., & Liu, Y. (2015). Analysis of auxiliary ribs in steel-concrete joint of hybrid girder. *Journal of Constructional Steel Research*, 112, 363–372.
- Ministry of Housing and Urban-Rural Development (MOHURD) of China. (2013). *Code for design of steel and concrete composite bridges, GB50917-2013*. Beijing. (In Chinese).
- Mirza, O., & Uy, B. (2010). Finite element model for the long-term behavior of composite steel-concrete push tests. *Steel & Composite Structures*, 10(1), 45–67.
- Naghavi, M., Rahnavard, R., Thomas, R. J., & Malekinejad, M. (2019). Numerical evaluation of the hysteretic behavior of concentrically braced frames and buckling restrained brace frame systems. *Journal of Building Engineering*, 22, 415–428.
- Nguyen, H. T., & Kim, S. E. (2009). Finite element modeling of push-out tests for large stud shear connectors. *Journal of Constructional Steel Research*, 65, 1909–1920.
- Oehlers, D. J., & Bradford, M. A. (1999). *Elementary behaviour of composite steel and concrete structural members*. London: Elsevier.
- Okada, J., Yoda, T., & Lebet, J. P. (2006). A study of the grouped arrangement of stud connectors on the shear strength behavior. *Structural Engineering/Earthquake Engineering*, 23(1), 75–89. (In Japanese).
- Ovuoba, B., & Prinz, G. S. (2016). Fatigue capacity of headed shear studs in composite bridge girders. *Journal of Bridge Engineering*, 04016094, 1–9.
- Qi, Y., Gu, Q., Sun, G., & Zhao, B. (2017). Shear force demand on headed stud for the design of composite steel plate shear wall. *Engineering Structures*, 148, 780–792.
- Rahnavard, R., Hassanipour, A., & Mounesi, A. (2016). Numerical study on important parameters of composite steel-concrete shear walls. *Journal of Constructional Steel Research*, 121, 441–456.
- Rahnavard, R., Hassanipour, A., Suleiman, M., & Mokhtari, A. (2017). Evaluation on eccentrically braced frame with single and double shear panel. *Journal of Building Engineering*, 10, 13–25.
- Rahnavard, R., Naghavi, M., Aboudi, M., & Suleiman, M. (2018). Investigating modeling approaches of buckling-restrained braces under cyclic loads. *Case Studies in Construction Materials*, 8, 476–488.
- Rahnavard, R., Taghikhajeh, M., Hassanipour, A., & Siahpolo, N. (2019). Parametric study of seismic performance of steel bridges pier rehabilitated with composite connection. *Journal of Structural & Construction Engineering*, 6(1), 98–113. (In Farsi).
- Ranzi, G., Leoni, G., & Zandonini, R. (2013). State of the art on the time-dependent behaviour of composite steel-concrete structures. *Journal of Constructional Steel Research*, 80, 252–263.
- Sellier, A., Multon, S., Buffo-Lacarrière, L., Vidal, T., Bourbon, X., & Camps, G. (2016). Concrete creep modelling for structural applications: Non-linearity, multi-axiality, hydration, temperature and drying effects. *Cement and Concrete Research*, 79, 301–315.
- Shao, C. Y. (2015). *Beam-type composite structure bridges*. Beijing: China Architecture & Building Press. (In Chinese).

- Shin, D. K., Dat, B. V., & Kim, K. (2014). Compressive strength of HPS box girder flanges stiffened with open ribs. *Journal of Constructional Steel Research*, 95, 230–241.
- Shin, D. K., Le, V. A., & Kim, K. (2013). In-plane ultimate compressive strengths of HPS deck panel with U-shaped ribs. *Journal of Structure & Construction Engineering*, 63, 70–81.
- Utescher, G. (1978). *Beurteilungsgrundlagen für Fassadenverankerungen*. Berlin-Wilmersdorf: Wilhelm Ernst & Sohn. **(In German)**.
- Wang, Q. (2013). Experimental research on mechanical behavior and design method of stud connectors. Ph.D. Dissertation. Shanghai: Tongji University. **(In Chinese)**.
- Xu, C., Sugiura, K., Wu, C., & Su, Q. (2012). Parametrical static analysis on group studs with typical push-out tests. *Journal of Constructional Steel Research*, 72, 84–96.
- Xu, G. P., Zhang, X. G., Liu, Y. Q., Liu, M. H., Zhao, C. H., & Liu, G. (2013). *Hybrid girder cable-stayed bridge*. Beijing: China Communications Press. **(In Chinese)**.
- Yang, F., Liu, Y., & Li, Y. (2018). Push-out tests on large diameter and high strength welded stud connectors. *Advances in Civil Engineering*, 2018(2), 1–12.

Publisher's Note Springer Nature remains neutral with regard to jurisdictional claims in published maps and institutional affiliations.